Direct visualization of emergent metastatic features within an *ex vivo* model of the tumor microenvironment

Libi Anandi, Jeremy Garcia[§], Libuše Janská[§], Josephine Liu[§], Manon Ros, Carlos Carmona-Fontaine*

Center for Genomics & Systems Biology, Department of Biology, New York University, New York, NY 10003, USA

*Correspondence: cf97@nyu.edu

[§]Equal contribution

ABSTRACT

Preventing tumor cells from acquiring metastatic properties would significantly reduce cancer mortality[1–5]. However, due to the complex nature of this process, it remains one of the most poorly understood and untreatable aspects of cancer[6–8]. Ischemia and hypoxia in solid tumors are requisite in metastasis formation – conditions that arise far from functional blood vessels and deep within tumor tissues[9,10]. These secluded locations impede the observation of pre-metastatic tumor cells and their interactions with stromal cells, which are also critical in the initiation of this process[11,12]. Thus, the initiation of metastasis has been incredibly difficult to model in the lab and to observe *in vivo*. We present an *ex vivo* model of the tumor microenvironment, called 3MIC, which overcomes these experimental challenges and enables the observation of ischemic tumor cells in their native 3D context with high spatial and temporal resolutions. The 3MIC recreates ischemic conditions in the tumor microenvironment and facilitates the co-culture of different cell types. Using live microscopy, we showed that ischemia, but not hypoxia alone, increases the motility and invasive properties of cells derived from primary tumors. These changes are phenotypic and can occur without clonal selection. We directly observed how interactions with stromal cells such as macrophages increased tumor invasion in conjunction with the effects of an ischemic microenvironment. Finally, we tested the effects of chemotherapy drugs under different metabolic microenvironments and found that ischemic tumor cells are more resistant to paclitaxel, possibly due to a metabolic resistance mechanism. Overall, the 3MIC is a cost-effective system that allows for the dissection of the complexity of the tumor microenvironment and direct observation of the emergence of metastasis, as well as the testing of treatments that may halt this process.

INTRODUCTION

Most cancer-related fatalities are directly or indirectly caused by metastases[5]. Thus, stopping pre-metastatic tumor cells from acquiring migratory and invasive properties could dramatically reduce cancer mortality[8]. And yet due to the complexity of this process, many of the mechanistic links between cell phenotypes and the disease remain unknown and untargeted. In fact, only a handful of drugs specifically target metastatic steps, and none are known to target or to prevent metastatic initation[6,7].

Multiple steps lead to the formation of successful metastases – each one with their own intricated regulatory mechanisms[1–4]. These diverse mechanisms include cell-autonomous changes such as oncogenic mutations as well as external factors including cell-cell interactions and metabolic conditions in the tumor microenvironment[12–16]. Moreover, many details remain unclear as it is almost impossible to predict when and where metastases emerge *in vivo.* Thus we are often limited to study metastasis via circulating tumor cells, biopsies, and *postmortem* analysis of metastases[17,18].

Cell metabolism is crucial in all steps of the metastatic process. The metabolism of tumor cells is as important as the metabolic composition of the local environments within the primary tumor and in future metastatic sites[16,19]. Among these environmental conditions, hypoxia is the determining factor in the emergence of metastatic cells[13–15] . Recent evidence suggests that most if not all metastatic cells experience low oxygen conditions before leaving the primary tumor[20]. Hypoxia in solid tumors arises in regions with poor blood perfusion and thus it does not occur alone but in combination with low nutrients and the accumulation of metabolic byproducts, a combination referred to as ischemia[21–25]. These metabolic conditions arise as the growth of some tumor cells separates others from nutrient sources. This separation makes these regions key in the initiation of metastasis and simultaneously almost impossible to access and observe *in situ*. Metastasis is also regulated by stromal cells that infiltrate solid tumors. Tumor-associated macrophages are some of the most abundant of these cells and they can promote and facilitate the metastatic process[11,26–29]. The inaccessibility of tumor niches where metastases emerge also impedes the visualization of tumor-stroma interactions and how they are modulated by metabolic factors in the tumor microenvironment.

52 All these factors make modeling metastasis *in vitro* and *in vivo* extremely difficult. Most tumor
53 models are better at recapitulating primary tumor growth than later stages of the disease[30,31].
54 And while some models allow studying spontaneous metastasis after resection of the primary
55 tumor, most studies deliver tumor cells directly into the bloodstream focusing on the final steps
56 of metastasis. Thus, due to unpredictable metastatic timing and the inaccessibility of niches
57 where metastases originate, studying and visualizing the initial steps of metastasis *in vivo* has
58 not been possible.

59 The complex set of conditions that drive metastatic initiation, means that there are very few *in*
60 *vitro* or *ex vivo* models of this process. These types of models however, could help with the
61 critical need for affordable and scalable experimental systems that model metastasis under
62 controlled conditions. Here we present an *ex vivo* model of the tumor microenvironment
63 specifically designed to visualize the transition from poorly motile primary tumor cells to
64 migratory metastatic-like cells. Our 3D Microenvironmental Chamber or 3MIC, can incorporate
65 key pro-metastatic factors such as stromal cell infiltration and tumor ischemia. In this system,
66 we can directly observe, track, and compare the evolution of well-nurtured and ischemic
67 multicellular 3D tumor structures using live microscopy and image analysis. While this device
68 only models a specific aspect of the metastatic process, we believe that its capability for
69 visualization of usually inaccessible microenvironments and its ease of use can boost our
70 understanding and treatment of early metastasis.

71 As a proof-of-principle, we show that ischemic conditions directly drive the emergence of
72 metastatic features including more efficient cell migration, increased extracellular matrix
73 degradation, and loss of epithelial features. By combining *in vivo* experiments with 3MIC
74 cultures, we can show that these are reversible phenotypic changes that do not require clonal
75 selection by hypoxia or other environmental challenges. We also show tumor interactions with
76 stromal cells such as macrophages and endothelial cells, increasing the pro-metastatic effects
77 of ischemia. Finally, we show that ischemic cells are more resistant to the anti-migratory effects
78 of paclitaxel even when adjusting by concentration and other potential explanations, suggesting
79 that ischemia provides resistance to this drug. In all, the 3MIC is an affordable and modular
80 culture system where different components of the tumor microenvironment – and their effect on
81 the first steps of metastasis – can be carefully dissected.

82 **RESULTS**

83 **A 3D *ex vivo* model for the direct visualization of ischemic tumor cells**

84 We wanted to directly visualize the effects of ischemia on the growth and movements of three-
85 dimensional (3D) tumor structures. For most of our experiments, we used small tumor organoids
86 referred to as tumor spheroids. Once formed, we embedded these tumor spheroids in a
87 collagen and laminin-rich extracellular matrix (ECM) scaffold and then observed their
88 development using an inverted spinning disk confocal with the environmental control required
89 for live microscopy.

90 We recently developed an *ex vivo* culture system where a 2-dimensional (2D) cell monolayer
91 generates spatial gradients of ischemia mimicking metabolic changes present in the tumor
92 microenvironment[32–34]. We thus first tested whether this system, named MEMIC, was
93 appropriate to study the impact of the metabolic microenvironment on 3D tumor structures. To
94 detect if tumor spheroids were experiencing ischemia, we engineered different epithelial tumor
95 cells to express a fluorescent hypoxia reporter (HRE-GFP). These cells also constitutively
96 express membrane mCherry (mCherry-CAAX)[32] to better visualize morphological changes. After
97 culturing these spheroids in the MEMIC, however, we were unable to detect GFP or any
98 changes in spheroid behavior or morphology along the MEMIC (Fig. S1A). It is possible that the
99 absence of gradients in these cultures was due to low cell density[32]. A typical 2D MEMIC culture
100 has about ~10^5 cells – which is about 100 times higher than the total cell number that we used
101 in our 3D cultures. Attempts to increase total cell number by adding more tumor spheroids,
102 resulted in large cell masses as neighboring clusters merged thus precluding us from examining
103 ischemic cells in detail (Fig. 1A). We thus concluded that the MEMIC was inadequate to study
104 the impacts of the metabolic microenvironment on 3D cultures.

105 We decided to develop a new culture system specifically designed to visualize the effects of
106 ischemia on multicellular tumor structures. We named this new system the 3D
107 microenvironment chamber or 3MIC. To test this system, we seeded a monolayer of tumor cells
108 derived from a mouse model of lung adenocarcinoma driven by $KRAS^{G12D}$ and $TP53^{-/-}$[35]
109 (referred to here as Lung KP cells). These cells also expressed HRE-GFP and mCherry-CAAX.
110 The principle behind the 3MIC is similar to the one in the MEMIC: a dense monolayer of cells is

111 restricted from accessing nutrients and oxygen from all but one side. This side acts as the
112 nutrient and oxygen source as it is open to a large volume of fresh media. This leads to the
113 formation of well-defined spatial gradients of metabolites (Fig. 1B; Fig. S1C). In the 3MIC
114 however, these cells are not the focus of our analyses and only act as nutrient and oxygen
115 consumers. These "consumer cells" grow on a coverslip at the top of the chamber so that they
116 do not obstruct the microscope's line of sight. We then place embedded tumor spheroids
117 beneath the consumer cell layers so that they impose a metabolic gradient on the entire culture
118 (Fig. 1B; Fig. S1C).

119 We first tested whether cells growing in the 3MIC produced gradients as they would in the
120 MEMIC. As in our previous experiment, we seeded Lung KP cells engineered to express HRE-
121 GFP and mCherry-CAAX. As expected, these cells displayed a strong gradient of GFP that
122 increased with the distance to the 3MIC's opening (Fig. S1B). We then repeated this experiment
123 but with ECM-embedded tumor spheroids growing below the monolayer of consumer cells. After
124 only 24h in the 3MIC, ischemic distal tumor spheroids showed high levels of GFP while
125 fluorescence levels in well-nurtured spheroids were negligible (Fig. 1C,D). As controls, we
126 embedded similar clusters in a 3MIC but without consumer cells and in this case we did not
127 detect GFP levels along the entire chamber (Fig. 1C,D). We obtained similar results with three
128 independently derived clones of Lung KP cells and in experiments using different cell lines and
129 with a different hypoxia reporter (Fig. S1D). As GFP levels in spheroids closely mirrored levels
130 in consumer cells we also observed dramatic morphological changes along the ischemia
131 gradient. Overall, these results show that consumer cells in the 3MIC form ischemic gradients
132 that determine the local metabolic microenvironment experienced by tumor spheroids. As
133 changes in the metabolic microenvironment of the 3MIC occur perpendicular to our imaging
134 path, we can observe how cells change with as much detail as needed. This simple geometrical
135 feature solved the accessibility to ischemic cells problem allowing us to visualize these cells with
136 the same ease as well-nurtured tumor structures.

137 **Hypoxia is required but not sufficient to increase invasive features in tumor spheroids**

138 The role of hypoxia in increasing tumor cell migration and invasion is well established[13,14,36–39]. It
139 is less clear, however, how these changes relate to changes triggered by ischemia – a more

140 complex challenge that is closer to the experience of tumor cells *in vivo*. Tracking individual
141 cells from dozens of tumor spheroids at different locations over several days is very data
142 intensive. To efficiently compare different treatments and conditions, we decided to use a rapid
143 metric reflecting the changes we observed in ischemic spheroids. We thus defined the
144 *invasiveness index* of a spheroid as the inverse of its circularity. Circularity, as a relationship
145 between area and perimeter, decreases in more irregular shapes. Thus, its inverse increases in
146 more protrusive and migratory 3D tumor structures (Fig. 1E).

147 We first tested whether hypoxia was *sufficient* to trigger morphological changes and increase
148 cell migration in 3D tumor spheroids. We compared spheroids cultured in regular petri dishes
149 incubated under different oxygen tensions (21% and 1%) with spheroids cultured in the 3MIC.
150 As in our previous experiments, cells in these spheroids expressed HRE-GFP and mCherry-
151 CAAX. As expected, tumor spheroids cultured in a hypoxic incubator increased GFP expression
152 to levels comparable to the brightest clusters in the 3MIC (Fig. S1E). Hypoxic spheroids were
153 slightly more invasive than spheroids cultured in regular incubators but not nearly as much as
154 ischemic spheroids in the 3MIC (Fig. 1E). In fact, hypoxic spheroids behaved similarly to well-
155 nurtured spheroids in the 3MIC suggesting that the latter may experience mild levels of
156 ischemia. We thus concluded that hypoxia alone only triggers minor morphological changes and
157 cannot fully recapitulate the changes that we observe in ischemic regions of the 3MIC.

158 To test whether hypoxia was *required* in altering spheroid morphologies, we took advantage of
159 the selective permeability of polydimethylsiloxane (PDMS)[32–34]. PDMS is permeable to oxygen
160 and other gases, but not to soluble metabolites. We thus constructed 3MICs using a PDMS
161 membrane molded into the shape of a glass coverslip. In these modified 3MICs, cells form
162 gradients of nutrients and metabolic byproducts, but oxygen rapidly equilibrates across the
163 PDMS membrane and thus there is no hypoxia (Fig. S1F). In this scenario, the effect of
164 consumer cells was minimal, with little increase in migration, and spheroids resembling control
165 cultures in the absence of consumer cells (Fig. 1F,G; Fig. S1F). Altogether, with these
166 experiments we conclude that hypoxia is *required* but not *sufficient* to increase the
167 morphological changes we observed in ischemic tumor spheroids. In addition, these results
168 highlight the advantage to consider complex metabolic challenges instead of single parameters
169 such as hypoxia.

170 **Ischemia stimulates persistent cell migration**

171 Lung KP spheroids growing in the 3MIC showed strong morphological differences along the
172 ischemic gradient. Distal ischemic spheroids lost their initial smooth and rounded shape
173 acquiring a ruffled, more protrusive morphology growing significantly in volume (Fig. 2A, Video
174 S1). We observed equivalent effects in spheroids from a panel of cell lines (Fig. S2A). This
175 increase in size – of up to 10-times the original volume – correlated with the distance to the
176 opening and thus to levels of ischemia (Fig. S2B). Control spheroids grown in 3MICs without
177 consumer cells, showed only a modest increase in growth (~2-fold), remained more smooth and
178 less protrusive, and none of these changes correlated with their position along the 3MIC (Fig.
179 2A; Fig. S2A,B). This growth was not driven by cell proliferation, the as detection of mitotic cells
180 via phospho-H3 immunostaining (Fig. S2C) or live fluorescent reporters (Fig. S2D; Video S2)
181 revealed a decrease rather than a proliferation increase in ischemic spheroids. Furthermore,
182 using live imaging we were able to detect a significant decrease in local cell density of ischemic
183 clusters (Fig. 2B; Video S3)[34] – suggesting that ischemic spheroids expand primarily by cell
184 dispersion (Fig. 2C).

185 Taking advantage of the high temporal and spatial resolution in live microscopy afforded by the
186 3MIC, we measured the migratory properties of individual tumor cells. To allow for accurate
187 automated cell tracking, we modified Lung KP cells to express a nuclear fluorescent protein
188 (H2B-YFP) and then we formed chimeric spheroids of these cells with isogenic Lung KP cells
189 expressing a different fluorophore (mCherry-CAAX; Fig. 2D; Video S4). We tracked hundreds of
190 cells from different spheroids along the gradient of ischemia. Analysis of nearly 900 tracks of
191 individual cells showed a large heterogeneity in their motility as some cells wandered near their
192 origin, while others moved large distances from their origin. On average however, cells from
193 ischemic clusters travelled further from their original location than cells from well-nurtured
194 clusters (Fig. 2E, Fig. S2E,F; Video S4). This increase in net displacement in ischemic cells was
195 not due to an increase in speed (Fig. S2G) but rather because they move more persistently than
196 well-nurtured cells (Fig, 2F). Consistent with the increase in persistence, Mean Square
197 Displacement (MSD) analysis of their migratory tracks showed that the movement of cells in
198 well-nurtured clusters was indistinguishable from a random walk (Fig. 2G, MSD constant,

199 σ=1.02). In contrast, the movement of ischemic cells was superdiffusive – meaning significantly
200 more directional than expected by random (Fig. 2G, σ=1.19; Fig. S2J).

201 To further explore these data, we defined *runners* as cells whose net displacement was greater
202 than an arbitrary distance threshold (50μm). At most values of this threshold, ischemic clusters
203 had about twice as many runners than well-nurtured spheroids or spheroids in chambers
204 without consumer cells (Fig. 2E,H; S2F). Interestingly, we observed a small directional bias in
205 the movement of runner cells away from ischemia as if they were moving toward nutrient
206 sources (Fig. 2H; Fig. S2H). However, this directional bias was very small and only significant
207 under a narrow definition of runner cells (Fig. S2I). We thus concluded that – at least in this
208 setting – metabolite and oxygen gradients do not act as strong orientation cues. Overall, our
209 data shows that ischemia leads to more persistent movements in three-dimensional tumor
210 cultures resulting in highly dispersive and invasive tumor spheroids.

211 **Ischemic tumor cells lose epithelial features and increase ECM degradation**

212 We then sought to determine specific cellular changes triggered by ischemia. Our cell migration
213 analyses showed that ischemic cells migrate more persistently but not faster than well-nurtured
214 cells and thus ischemia does not act as a chemokinetic factor. We also did not find strong
215 evidence of metabolites acting as chemotactic signals. We thus thought that ischemia may
216 trigger structural changes such as diminishing cell-cell adhesion and their affinity to the ECM.

217 The increase in MSD shown in Figure 2G, provides insight into the impact of ischemia on cell
218 movements. From a statistical point of view, it shows that on average these cells keep moving in
219 the same direction for longer periods of time – even if this direction is random[40]. In other words,
220 these data suggest that the movements of ischemic cells are less constrained for longer than
221 well-nurtured tumor cells. Typically, these constraints can come from the ECM scaffolding and
222 from cell-cell adhesions[41,42]. We thus tested whether ischemic spheroids increase ECM
223 degradation, reduce cell-cell adhesion, or both. As a first approach to measure ECM
224 degradation, we used a well-established quantitative ECM degradation assay[43]. Briefly, a layer
225 of proteins – in this case collagen – is laid over a coverslip coated with fluorescent gelatin. More
226 invasive clusters will break down the collagen network, and eventually, the labelled gelatin
227 resulting in local loss of fluorescence (Fig. 3A). With this assay, we determined that ischemic

228 spheroids increased ECM degradation and so do ischemic consumer cells (Fig. 3B; Fig. S3A).
229 As an orthogonal approach, we cultured tumor spheroids in DQ-Collagen – a labeled but
230 quenched form of collagen that fluoresces when cleaved[44]. Again, in this assay ischemic
231 clusters showed a much higher ECM degradation (Fig. S3B) and the fluorescence of DQ-
232 Collagen colocalized with cell structures that protruded into the ECM (Fig. S3C).

233 As we showed above, cells from ischemic clusters rapidly disperse a process that requires
234 reducing cell-cell adhesion. The cell adhesion molecule E-Cadherin (E-Cad) has a key role in
235 the integrity of epithelial tissue[45,46]. As epithelial-derived carcinoma cells, our Lung KP cells,
236 display well-defined cell-cell adhesions lined by high levels of E-Cad (Fig. 3C). There is
237 evidence that metabolic conditions in the tumor microenvironment decrease epithelial features
238 in carcinomas[37,39,47–51], including our data showing that mammary tumor cells in the MEMIC
239 dramatically reduce CDH1 levels[32]. We thus asked whether ischemic spheroids also decrease
240 CDH1-mediated cell-cell adhesion. Using CDH1 immunofluorescent staining we observed that
241 tumor spheroids in the 3MIC decreased CDH1 levels in correlation with ischemia (Fig. 3C,D).
242 We observed a similar trend using a fluorescent CDH1 live reporter (Fig. S3D). While spheroids
243 decreased these epithelial features, we did not see signs of the acquisition of a mesenchymal
244 fate such as increased vimentin levels, and we thus concluded this is not EMT. Taken together,
245 these results show that ischemic cells decrease epithelial adhesion and degrade their
246 surrounding ECM more efficiently.

247 **A model of persistent tumor migration in the absence of directional cues**

248 While the evidence that hypoxic, *i.e.* ischemic, tumor cells metastasize more *in vivo* is well-
249 established[11,13,15,20], it is at the same time puzzling. If ischemic cells are located – by definition –
250 far from blood vessels then, how do these distal cells move through the tumor, invade the ECM,
251 and reach the bloodstream? An appealing hypothesis is that nutrients or oxygen act as
252 directional cues that orient the movements of ischemic cells. However, our data do not support
253 this hypothesis (Fig. 2H; Fig. S2H). We thus asked whether our other observations – more
254 persistent movement, decreased epithelial adhesion and more efficient invasion of the ECM –
255 would allow ischemic cells to move through surrounding well-nurtured cells and invade the
256 ECM.

257 We decided to address this question conceptually using a Cellular Potts Model (CPM)[52,53].
258 CPMs are a computational framework frequently used to solve problems of differential cell
259 adhesion and sorting in morphological processes[54]. In CPMs, any number of 'cell types' exist on
260 a grid and have different affinities for each other and for their surrounding substrate. In CPMs,
261 high affinity contacts have a lower surface energy and thus they are more stable. In contrast,
262 low cell-cell or cell-substrate affinities are represented as highly energetic and unstable contacts
263 (Fig. 3E). At every simulated time point or Monte Carlo Step (MCS), the CPM tries to minimize
264 the energy of the system resulting in changes in cell shape, localization, etc. according to local
265 energy levels[52,53]. In our model, we defined small tumors formed by two cell types: *core*
266 (ischemic) and *cortical* (well-perfused) cells according to their positions at the beginning of the
267 simulation. Our specific goal was to test whether changes in cell-cell and cell-substrate
268 adhesion would allow core cells to move through cortical cells and eventually invade into the
269 surrounding ECM (Fig. 3E).

270 We modelled the reduced levels of E-Cad we observed in ischemic cells as an increase in the
271 surface energy between core cells (decreasing their stability). Energy levels were set to ensure
272 that the adhesion between core cells was low, between cortical cells was high, and intermediate
273 between the two cell types. We tested a range of affinity parameters obtaining similar qualitative
274 results as long as we kept these relationships. Implementation of these changes in adhesion
275 resulted in clusters where core cells mixed with cortical cells but there was no invasion into their
276 surroundings (Fig. 3F; Video S5). To model the increased ECM invasion in ischemic cells, we
277 gave core cells a higher affinity for the surrounding ECM than cortical cells. This feature alone,
278 produced poor mixing between populations and some invasion into the surrounding ECM (Fig.
279 3F; Video S5). However, the overall movement of these cells was random and did not show the
280 persistence we observed in our experiments (Fig. 3F; S3E).

281 We then combined these two rules – core cells with decreased cell-cell adhesion and increased
282 cell-ECM adhesion. In this case, ischemic core cells moved through layers of well-perfused cells
283 and rapidly dispersed through the surrounding ECM (Fig. 3F; Video S5). These virtual cell
284 movements were remarkably close to the movements of our experimental cells. For example,
285 tracks of core and cortical cells in the model (Fig. 3G), resembled the movements of ischemic
286 and well-nurtured cells, respectively (compare with Fig. S2F). Most strikingly, core cells with

287 these two rules increased their MSD and they did so in the same order of magnitude as
288 experimental cells in the 3MIC (compare Fig. 3H and Fig. 2G). Altogether these data suggest
289 that increasing the affinity for the ECM and decreasing cell-cell adhesion is sufficient for the
290 spontaneous emergence of directional movements and the dispersion of core cells into distal
291 ECM surroundings – even in the absence of explicit directional cues.

292 **Pro-metastatic features induced by ischemia are reversible**

293 Hypoxia and ischemia are known to trigger transcriptional and other phenotypic changes that
294 increase cell migration and invasion[13–15,55,56]. But recent evidence suggests that hypoxic
295 environments may select for more aggressive clones.[20] The brief timescale of our 3MIC
296 experiments (~24-72h) neglects any significant role for selection and underscores the
297 importance of phenotypic adaptations to ischemia. *In vivo* however, time scales are much
298 longer, which may allow ischemia to select for more migratory clones. We hypothesized that, if
299 ischemic cells are selected to be more migratory *in vivo*, they should display a higher migratory
300 phenotype in the 3MICs – irrespective of their location. To test this hypothesis, we injected Lung
301 KP expressing GFP-HRE cells into the flank of syngeneic mice. After 2 weeks, tumors were
302 extracted and dissociated into single cells. Using flow cytometry, we sorted ischemic from non-
303 ischemic cells according to their GFP levels (Fig. S4A). From these sorted cells, we generated
304 tumor spheroids, which we then cultured into separated 3MICs (Fig. 4A; Fig. S4B). As shown in
305 figure 4C, the increase in cell migration and invasion strongly correlated with their distance to
306 the opening but did not depend on whether spheroids came from low or high GFP tumor regions
307 (Fig. 4B,C). Importantly, these spheroids did not show any increase in migratory properties
308 when cultured in 3MICs without consumers – regardless of where in the tumor they came from
309 (Fig. S4C,D). Altogether, these results show that the pro-metastatic features produced by
310 ischemia are reversible phenotypic changes and suggest that, at least in this system, they do
311 not require clonal selection.

312 **Reconstruction and visualization of more complex microenvironments**

313 Solid tumors are infiltrated with a variety of stromal and immune cells[11]. Among these different
314 cell types, tumor-associated macrophages (TAMs) are one of the most abundant and can
315 increase, tumor progression, metastasis, and mortality[26–29,57–59]. TAMs can recruit endothelial

316 cells and help to orchestrate the vascularization process required for tumor growth and
317 metastasis. We recently showed that a combination of hypoxia and high lactic acid typically
318 found in ischemic tumor regions, activate the ERK/MAPK in macrophages who then secrete
319 VEGFA and induce tube-like morphogenesis in endothelial cells[33]. Since this process only
320 occurs under ischemia, it provides a great system to test the co-culturing capabilities of the
321 3MIC.

322 We first generated endothelial spheroids from SVEC4-10 cells (referred as SVECs). We then
323 co-cultured these spheroids in 3MICs filled with ECM containing a suspension of bone marrow-
324 derived macrophages (BMDMs), or ECM without BMDMs. In the absence of macrophages,
325 clusters of endothelial cells remained mostly rounded – even in the presence of consumer cells
326 and regardless of their location along the ischemic gradient (Fig. 5A; Video S6). In the presence
327 of macrophages however, endothelial cells extended away from the clusters and sprouted into
328 the ECM (Fig. 5A; Video S6). Importantly, endothelial clusters in co-cultures without consumer
329 cells did not show major morphological changes, indicating that in the absence of strong
330 ischemia, macrophages do not have a strong pro-angiogenic role (Fig. S5A). Consistently, tube-
331 like morphogenesis only occurred within ischemic regions of the 3MIC (Fig. 5A; Video S6).
332 Consistent with previous evidence[29,33], inhibition of VEGF signaling completely abrogated
333 macrophage-induced endothelial sprouting (Fig. 5B; Fig. S5B). Altogether, these results confirm
334 that ischemic macrophages induce tube-like morphogenesis in endothelial cells in a VEGF-
335 dependent manner.

336 After verifying that the 3MIC is well-suited for co-culture experiments, we conducted similar
337 experiments, but this time using Lung KP tumor spheroids and BMDMs. In these experiments,
338 ischemia alone or the presence of macrophages – even in well-nurtured regions – increased cell
339 migration and ECM invasion (Fig. 5C). However, we also observed a strong synergy between
340 ischemia and the presence of macrophages increasing cell migration and invasion (Fig. 5C) and
341 decreasing E-Cad levels (Fig. 5D; Fig. S3D). A fascinating observation was that tumor cells
342 from ischemic spheroids extend protrusions towards macrophages appearing to physically drag
343 them into the tumor cell cluster (Video S7).

344 Finally, to demonstrate that it is easy to increase the cellular complexity in the 3MIC, we co-
345 cultured all three cell types. In this case, we formed mixed SVEC/Lung KP spheroids embedded
346 in ECM containing BMDMs (Fig. 5E; Video S8). Again, here it is possible to observe the strong
347 synergy of the combination of macrophage and metabolic signals.

348 **Ischemic cells are more resilient to anti-migratory drugs**

349 Witnessing the transition from poorly migratory tumor cells to highly invasive ones, provides a
350 unique opportunity to test drugs that directly target metastatic initiation. As a proof of principle,
351 we tested the effects of paclitaxel on migratory tumor spheroids. Paclitaxel stabilizes
352 microtubules leading to mitotic arrest and cell death[60]. At lower concentrations however,
353 paclitaxel inhibits cell migration without a significant effect in cell viability[61,62]. We established
354 that concentrations ranging from 30-200nM produced a complete inhibition of cell movements in
355 well-nurtured tumor spheroids, while having a negligible effect on cell viability (Fig. S6A,B).
356 Surprisingly, paclitaxel completely failed at inhibiting the migration of ischemic cells (Fig. 6A,B).

357 The lack of response in ischemic spheroids may result from three possible mechanisms. First,
358 drug levels may decrease due to passive diffusion along the 3MIC. We quickly ruled out this
359 explanation because control spheroids in 3MICs without consumers are not resistant to the
360 effects of paclitaxel (Fig. 6A,B). A second mechanism is that consumer cells accentuate any
361 potential drug dilution due to diffusion by consuming or actively degrading paclitaxel. To test this
362 alternative, we need to visualize or measure local levels of paclitaxel and compare how they
363 change along 3MICs with or without consumer cells. Fortunately, fluorophore-conjugated
364 paclitaxel analogues are routinely used as probes to label microtubules. Thus, we can directly
365 visualize the microtubules of cells exposed to known quantities of these analogues and
366 determine how they change along 3MICs. We first treated tumor spheroids in the 3MIC with
367 30nM of a labelled paclitaxel analogue (docetaxel-Cy5). As shown in Fig. 6C, fluorescence
368 levels progressively decreased in more distal spheroids, but they did so at the same rate in
369 3MICs with or without consumer cells (~7% *per* mm, Fig. 6C,D; Fig. S6C). We then repeated
370 these experiments while increasing the levels of paclitaxel to 150nM. These levels even after
371 accounting for the effects of diffusion should ensure that the most distal spheroids experience
372 levels of paclitaxel that inhibit migration in well-nurtured spheroids (estimations: 45nM at 10mm

373 and 24nM at 12mm). Even under these conditions, ischemic clusters increased pro-metastatic
374 features such as increased cell migration and invasion (Fig. S6D). Together these data show
375 that ischemia reduces the effects of paclitaxel. We thus conclude that the reason why ischemic
376 spheroids do not respond to paclitaxel treatment is not due to drug penetration or diffusion
377 suggesting a true paclitaxel resistance mechanism induced by the metabolic microenvironment
378 invasion (Fig. 6E). Altogether these experiments show that the 3MIC recapitulates key features
379 of the tumor microenvironment, allows for the imaging ischemic cells that are hidden to
380 conventional techniques, and permits one to test the effects of drugs in the presence of stromal
381 cells in order to untangle different factors affecting the emergence of metastatic features.

382 **DISCUSSION**

383 Animal models are a fundamental tool to study the complex and heterogeneous tumor
384 microenvironment[31,63]. However, the complexity of animal physiology challenges the
385 assessment of the contribution of different variables, and their use for large experiments is
386 severely impossible due to economical and ethical concerns[64,65]. On the other side of the
387 spectrum, conventional *in vitro* experiments offer much better experimental control and can be
388 easily used in high throughput approaches. However, these cultures do not model the metabolic
389 heterogeneity and other essential features of the tumor microenvironment. These challenges
390 have been particularly evident when studying the emergence of cancer metastasis[6–8].

391 In this article we described the design and implementation of the 3MIC – an *ex vivo* culture
392 system that allows us to track pre-metastatic cells and their transition to metastatic-like
393 migratory cells in complex 3D tumor cultures. This system overcomes the visualization
394 limitations by decoupling the cells of interest from the cells that create nutrient-deprived
395 conditions.

396 As expected, we can show that hypoxia in the 3MIC is important for the emergence of
397 metastasis. However, the more complex environments created in the 3MIC show that additional
398 metabolic conditions in the tumor microenvironment point to and are also required for
399 metastasis. Consistent with our data, a recent paper showed that nutrient deprivation triggers
400 the release of pro-migratory cytokines[66]. Similarly, there is accumulating evidence that cell
401 metabolism and metabolic signals including nutrients such as pyruvate[16], are critical in
402 determining the likelihood, number, and destination of metastasis[16,19]. These data, showing how
403 tumor behavior is modulated by a complex mix of metabolic signals, indicates that there is an
404 urgent need for a better characterization of ischemia.

405 Our data shows that ischemia leads to more directional cell movements. Mechanistically, we
406 show that ischemia leads to a decrease in epithelial adhesion and increased degradation of the
407 extracellular matrix. While our combination of experiments and simulations do not prove that
408 lower cell-cell adhesion and increased invasion in ischemic cells are the only way ischemic cells
409 can escape a cell mass, they show that these mechanisms may be sufficient to do so.

410 While some of our observations share features with the process of epithelial-to-mesenchymal
411 transition (EMT), we avoided using this term for several reasons. First, we only observed a
412 decrease in epithelial features without an increase in mesenchymal markers such as vimentin.
413 Second, the role of E-Cadherin in EMT is a lot clearer during development than in cancer[67,68],
414 where its role remains controversial[49,69].

415 At the single cell level, ischemia increases cell persistence without the need of an intrinsic
416 mechanism for cell polarity and directional cell migration. However, we observed a small bias
417 towards higher nutrients in the direction of cell movements. While in our settings these
418 differences were close to statistical significance thresholds, it would be consistent with
419 widespread examples of starvation and nutrient-driven chemotaxis in prokaryote and eukaryote
420 cells[70,71]. Interestingly, the key nutrient sensor mTORC2 is critical in neutrophil chemotaxis. Still,
421 additional experiments will be needed to establish chemotaxis as a potential strategy for nutrient
422 scavenging in tumors.

423 Recent evidence shows that tumor hypoxia can act as an evolutionary pressure that selects for
424 tumor clones that are more resilient to stressors such as reactive oxygen species[20,49,72].
425 However, our data shows that hypoxia and ischemia can alter cells directly without the need of
426 clonal selection. These two ideas are not in conflict and our experimental conditions are not free
427 of caveats. Most likely the acquisition of metastatic features in patients occurs by a combination
428 of selection and opportunistic adaptations to the tumor microenvironment.

429 The direct visualization of tumor-stroma interactions afforded by the 3MIC has unique
430 advantages. For example, we were very surprised to observe how much of the movement of
431 macrophages towards tumor structures, seemed to be driven by tumor cells, dragging
432 macrophages into their clusters (see for example Video S7). It is possible then, that part of the
433 immune infiltration of tumors is driven by physical recruitment by tumor cells. While we are not
434 aware of reports about this behavior *in vivo*, this may be due to the lack of other techniques for
435 the direct visualization of the tumor microenvironment highlighting the contributions the 3MIC
436 may bring to the community.

437 Poor vascularization in tumors hampers drug delivery to ischemic cells where concentration is
438 lowered by diffusion through tissues[73]. Thus, *in vivo* it is difficult to discern whether a decrease

439 in drug response is due to lower drug concentration or due to intrinsic changes in cells that
440 make them more drug resistant. The 3MIC however allows for the separation of these effects.
441 While the resistance to paclitaxel we show here is interesting, we chose this drug primarily
442 because its use as a microtubule probe allowed us to estimate local concentrations. However,
443 we plan to use the 3MIC to screen for genetic and pharmacological perturbations that may
444 prevent the increase of migratory behaviors triggered by ischemia.

445 The microfabrication of the 3MIC is easy and affordable only requiring a conventional 3D printer.
446 Also, this system seamlessly integrates existing co-culture and *ex vivo* protocols already used in
447 other laboratories. Thus, we invite the research community to use the 3MIC to study and rapidly
448 assess the effects of different factors on metastasis before moving to expensive *in vivo* models.

449 **METHODS**

450 **Cell culture**

451 Lung KP clones and Lung KPK clones were derived in the $KRAS^{G12D}/TP53^{-/-}$ and and
452 $KRAS^{G12D}/TP53^{-/-}$ / Keap $1^{-/-}$lung adenocarcinoma model, respectively, developed and kindly
453 shared by Dr. Thales Papagiannakopoulos. MCF10A, MCF7, DID1 cells and SVEC-4-10 cells
454 were purchased from ATCC. C6-HRE-GFP cells were a kind gift from Dr Inna Serganova
455 (Memorial Sloan Kettering Cancer Center, New York, NY, USA). Cells were cultured in High
456 Glucose DMEM (Gibco, #11965-092) supplemented with 10% Fetal Bovine Serum (FBS;
457 Sigma-Aldrich, #F0926) at 5% CO_2 and 37°C. Lung KP cells stably expressing a hypoxia
458 reporter (pLenti-5XHRE-GFP, Addgene #128958, denoted here as HRE-GFP), cell membrane
459 marker (pLenti-mCherry-CAAX, Addgene #129285), E-cadherin reporter (pHAGE-E-cadherin-
460 RFP, Addgene #79603), cell cycle reporter (pBOB-EF1-FastFUCCI-Puro, Addgene #86849),
461 LV-YFP (Addgene #26000), and pLenti-H2B-iRFP720 (Addgene #128961) were generated
462 using standard lentivirus mediated stable cell lone preparation protocols. H2B-mCherry was
463 cloned by removing YFP from the LV-YFP vector using BamHI and KpnI restriction enzymes.
464 The linearized vector containing H2B was then ligated with mCherry using SLIC[74].

465 **Formation of 3D tumor spheroids**

466 Spheroids of cells were formed via hanging drops following standard protocols [75]. Briefly, cells
467 were dissociated into a single-cell suspension of 10^4 cells/ml. The cell suspension was
468 distributed into 20μl droplets onto the lid of a Petri dish. The base of the dish was filled with PBS
469 (Gibco, #14040-133) or distilled water to prevent droplet evaporation during the incubation time.
470 The lid was then inverted onto the dish and incubated for 96 hours, to ensure the formation of
471 compact spheroids. Typically, we cultured ~50 spheroids in each 3MIC chamber.

472 **Isolation and differentiation of BMDMs**

473 Bone marrow-derived macrophages (BMDMs) were extracted from C57BL/6 mice following
474 standard protocols[33,34]. Following isolation of the bone marrow, cells were cultured in low
475 attachment culture dishes (VWR, #25384-342) in High Glucose DMEM supplemented with 10%
476 FBS and 10ng/mL Recombinant Mouse CSF-1 (R&D Systems, #416-ML) for 7 days.

477 **Establishment of tumor-derived clones**

478 Approximately $5x10^4$ cells Lung KP cells, stably expressing pLenti-5XHRE-GFP and pLenti-
479 mCherry-CAAX were injected subcutaneously into C57BL/6 mice and grown for 14 days.
480 Tumors were then extracted and dissociated using a solution containing of 2U/ml Dispase and
481 4mg/ml Collagenase IV. Cells were then sorted using FACS according GFP levels. GFP-
482 positive and negative cells were grown separately as clusters using the hanging drop method
483 described above.

484 **3D printing and microfabrication**

485 To create the framework of 3MIC fused filament fabrication was used. Designing of the
486 framework was done using openSCAD (https://openscad.org). 3MICs were printed in two parts
487 that were later assembled: the main framework and the upper coverslip holder (where consumer
488 cells are grown). These parts were printed in an Ultimaker 3B printer using Black PLA filament.
489 Alternatively, the framework can be printed using Stereolithography (SLA) printers. In this case,
490 the entire framework (the upper coverslip holder and main framework) can be printed as one
491 unit. We used Formlabs's Dental SG resin to print the framework on Form 3 (Formlabs). The
492 uncured resin was removed from the prints by washing them in isopropanol for 1 h and further
493 post-curing it with UV irradiation heated at 60°C. A glass coverslip (VWR, No. 1, 22x60mm,
494 #48393-070) was glued to the base of the main framework using a UV-curable adhesive
495 (Norland Products, NOA68) using a long-wave UV lamp (MelodySusie, DR-5401). Then, the
496 coverslip holder fragment was glued onto the glass coverslip. Finally, the assembled 3MIC was
497 sterilized in a short-wave UV lamp chamber (Meishida, CM-2009) for 15 minutes.

498 **Culture of tumor spheroids in the 3MIC**

499 To prepare the layer of consumer cells, 24hrs before the day of the experiment, a coverslip
500 (VWR, No. 2, 18x18 mm, #48366-045) was coated with Poly-D-lysine (Sigma-Aldrich, #P6407)
501 to aid adherence of cells to the glass surface. Cells were detached using trypsin and diluted into
502 a cell suspension of a density of $3.5x10^5$ cells/mL for faster dividing cells and 10^6 cells/mL for
503 slower dividing cells. The coverslip was placed into a well of a 6-well dish and covered with 1mL
504 of the cell suspension. The coverslip was incubated overnight at 37°C to let the cells adhere to

505 the coverslip. On the day of the experiment, the spheroids were collected from the Petri dishes
506 by inverting the lid and gently flushing all the spheroids with DMEM supplemented with 10%
507 FBS using a 5mL serological pipette. The spheroid containing suspension was collected and
508 centrifuged at 50G for 10-15 minutes. Meanwhile, a thin bed of 110μL ECM was made in the
509 3MIC – here, we used either 2.2mg/mL rat tail Collagen (Corning, #354236) – or 2:3 mix of
510 Matrigel and 1.6mg/ml of rat tail Collagen I and incubated at 37°C for 20 mins to allow the
511 polymerization of the ECM. Spheroids were resuspended in about 110μL of ECM and
512 immediately transferred onto the polymerized ECM bed. The ECM with spheroids was
513 polymerized at 37°C for ~30 minutes. With the help of forceps, the coverslip containing the
514 consumer cells was inverted and inserted into the slot of the coverslip holder. The 3MIC was
515 then gently filled with 1.25mL of media, avoiding trapping bubbles underneath the consumer
516 coverslip. Control wells are assembled in the same way, but the top coverslip has no consumer
517 cells.

518 **Collagen degradation assay**

519 To investigate the invasive potential of cells across the gradient, the ECM was mixed with DQ-
520 collagen, type I From Bovine Skin, Fluorescein Conjugate (Invitrogen, #D12060) at a final
521 concentration of 25μg/ml. This ECM was used to prepare the bed and embed the spheroids as
522 well. The extent of degradation of the matrix was determined by measuring the fluorescence
523 intensity of cleaved collagen.

524 **Gelatin degradation assay**

525 Glass coverslips were coated with gelatin from pig skin, Oregon Green 488 Conjugate (Thermo
526 Fisher Scientific, #G13186), by inverting coverslips on 20µl drops of fluorescent gelatin
527 (1mg/ml) and incubating for 20 minutes. The coverslips were then lifted, excess liquid drained,
528 and inverted on 40µl drops of 0.5% glutaraldehyde for fixation. The coverslips were then
529 washed with PBS and glued onto the PLA frame using the UV-curable adhesive (Norland
530 Products, #NOA68) and cured in a long-wave UV lamp (MelodySusie, #DR-5401) for 15
531 minutes. The cured coverslip was then UV-sterilized and used for the experiment. Briefly, the
532 spheroids were collected from the hanging drops and centrifuged and resuspended in 100µl of
533 media. The spheroid solution was carefully placed on the coated coverslips and incubated for

534 30-60 minutes to allow the spheroids to settle down. After ensuring that there are no floating
535 spheroids, the consumer coverslip was transferred into the 3MIC and the remaining 1.4ml of
536 media was added. The 3MICs were incubated at 37°C, for 24 hours. After 24 hours, the 3MICs
537 were fixed using 4% paraformaldehyde (PFA) for 10 mins and imaged using 10X objective of
538 Nikon Eclipse Ti2-E spinning disk confocal microscope.

539 **Microscopy**

540 Microscopic images were captured using a 10x objective of Nikon Eclipse Ti2-E spinning disk
541 confocal microscope, at fixed timepoints or set up for time-lapse microscopy. For time-lapse
542 microscopy, cells were maintained at 37°C using a stage top incubator (Tokai Hit, #INUCG2-
543 KRi) and the chamber was connected to a humidified mixed gas source (5% CO_2). Spheroids
544 from different regions of the 3MIC were imaged at suitable time-intervals in different fluorescent
545 channels. Typically, we imaged ~10 spheroids per 3MIC every 15-30 mins for 24h.

546 **Immunofluorescence**

547 Spheroids within the 3MIC were fixed using 4% PFA (Affymetrix, #19943) for 10 minutes at
548 room temperature and washed four times with PBS. Cultures were permeabilized using PBS
549 containing 0.5% (vol/vol) Triton-X-100 (Sigma-Aldrich, #T8787) for 20 minutes and washed
550 three times with PBS. Slides were blocked in 10% FBS in immunofluorescence (IF) buffer (0.3M
551 glycine in PBS) for 60 minutes at room temperature. Primary antibodies were diluted at 1:200 in
552 the same blocking solution. We used anti-phospho-H3 (Cell Signaling Technologies, #9706), E-
553 cadherin (BD Bio Sciences, #610182), and CD45 (R&D, #AF114) antibodies. 3MICs were
554 incubated with primary antibodies overnight at 4°C, then washed with IF buffer and incubated
555 overnight at 4°C with secondary antibodies also diluted in blocking solution at 1:200. Cultures
556 were then washed and counterstained with 0.5µg/mL Hoechst 33342 in PBS (Invitrogen,
557 #H1399).

558 **Image analysis**

559 Automated cell tracking was conducted as previously described[34]. Persistence is defined as the
560 ratio between the net displacement of a cell over its trajectory. We estimated the local cell
561 density using a method based on the Delaunay triangulation of neighboring cells[33,34]. Per cell,

562 per spheroid, and population levels of florescence were estimated using custom image analysis
563 software as previously described[32].

564 **Cellular Potts Model (CPM) simulations**

565 Simulations were conducted using a MATLAB CPM implementation[76]. Adhesion between core
566 (C1) and cortical (C2) cells were implemented as:

567 $$J_{C1,C1} > J_{C1,C2} > J_{C2,C2}$$

568 Where $J_{i,j}$ is the surface energy at every contact point between the two cells[53]. This relationship
569 modeled the decrease in E-Cad levels in ischemic cells. The differential affinity for the ECM in
570 core cells was simulates as:

571 $$J_{C1,ECM} < J_{C2,ECM}$$

572 The CPM was implemented in a 200x200 grid with 100 initial cells and run for $1{,}28 \times 10^8$ Monte
573 Carlo Simulation steps. MATLAB routines to run the simulations are available upon request.

574 **Statistics**

575 We conducted at least three biological replicates of all experiments. Unless noted, we used two-
576 tailed t-student tests to estimate p-values between two conditions and Pearson's linear
577 coefficient when testing correlations. For multiple comparisons, we used one-way ANOVA
578 followed by a Tukey-Kramer test. In all plots, error bars show standard deviation from the mean.
579 In boxplots, center lines show the median and box edges show 75th and 25th empirical quartiles
580 of the data.

581 **ACKNOWLEDGEMENTS**

582 We thank all members of the Carmofon Laboratory for critical discussions about this project and
583 the manuscript. This work was supported by awards to CC-F from the National Cancer Institute
584 of NIH (DP2 CA250005) and the American Cancer Society (RSG-21-179-01-TBE). CC-F is a
585 Pew Scholar in the Biomedical Sciences, supported by The Pew Charitable Trust (00034121).
586 JG was partially funded by a NIH Training Grant (1T32GM132037-01).

Authors contributions: Concept and experimental design CC-F with help from LA. Experiments by LA, JG, JL, MR, and C-CF. Image analysis: CC-F, LA, and LJ. Mathematical modeling: CC-F. Manuscript written by CC-F with feedback and contributions from all authors.

Competing interests: The 3MIC is an embodiment of a patent application to which CC-F is an inventor.

Data and materials availability: All data is available in the manuscript or the supplementary materials. Original raw files and analysis software are available upon request. Use of the 3MIC requires a Material Transfer Agreement and it is free for non-commercial and academic purposes.

ADDITIONAL INFORMATION

Supplementary information is available for this paper. Correspondence and requests for materials should be addressed to CC-F.

1. Massagué, J. & Obenauf, A. C. Metastatic colonization by circulating tumour cells. *Nature* **529**, 298–306 (2016).

2. Lambert, A. W., Pattabiraman, D. R. & Weinberg, R. A. Emerging Biological Principles of Metastasis. *Cell* **168**, 670–691 (2017).

3. Welch, D. R. & Hurst, D. R. Defining the Hallmarks of Metastasis. *Cancer Res* **79**, 3011–3027 (2019).

4. Chaffer, C. L. & Weinberg, R. A. A perspective on cancer cell metastasis. *Science (1979)* **331**, 1559–1564 (2011).

5. Siegel, R. L., Miller, K. D., Fuchs, H. E. & Jemal, A. Cancer statistics, 2022. *CA Cancer J Clin* **72**, 7–33 (2022).

6. Anderson, R. L. *et al.* A framework for the development of effective anti-metastatic agents. *Nature Reviews Clinical Oncology 2018 16:3* **16**, 185–204 (2018).

7. Fontebasso, Y. & Dubinett, S. M. Drug Development for Metastasis Prevention. *Crit Rev Oncog* **20**, 449–474 (2015).

8. Ganesh, K. & Massagué, J. Targeting metastatic cancer. *Nature Medicine 2021 27:1* **27**, 34–44 (2021).

9. Makohon-Moore, A. P. *et al.* Precancerous neoplastic cells can move through the pancreatic ductal system. *Nature 2018 561:7722* **561**, 201–205 (2018).

10. Klein, C. A. Parallel progression of primary tumours and metastases. *Nature Reviews Cancer 2009 9:4* **9**, 302–312 (2009).

11. Quail, D. F. & Joyce, J. A. Microenvironmental regulation of tumor progression and metastasis. *Nat Med* **19**, 1423–1437 (2013).

12. Massagué, J. & Ganesh, K. Metastasis-Initiating Cells and Ecosystems. *Cancer Discov* **11**, 971–994 (2021).

13. Rankin, E. B. & Giaccia, A. J. Hypoxic control of metastasis. *Science* **352**, 175–80 (2016).

14. Gilkes, D. M., Semenza, G. L. & Wirtz, D. Hypoxia and the extracellular matrix: drivers of tumour metastasis. (2014) doi:10.1038/nrc3726.

15. Nobre, A. R., Entenberg, D., Wang, Y., Condeelis, J. & Aguirre-Ghiso, J. A. The Different Routes to Metastasis via Hypoxia-Regulated Programs. *Trends Cell Biol* **28**, 941–956 (2018).

16. Bergers, G. & Fendt, S. M. The metabolism of cancer cells during metastasis. *Nature Reviews Cancer 2021 21:3* **21**, 162–180 (2021).

17. Iacobuzio-Donahue, C. A. *et al.* Cancer biology as revealed by the research autopsy. *Nature Reviews Cancer 2019 19:12* **19**, 686–697 (2019).

18. Ring, A., Nguyen-Sträuli, B. D., Wicki, A. & Aceto, N. Biology, vulnerabilities and clinical applications of circulating tumour cells. *Nat Rev Cancer* (2022) doi:10.1038/S41568-022-00536-4.

19. Lehúede, C., Dupuy, F., Rabinovitch, R., Jones, R. G. & Siegel, P. M. Metabolic plasticity as a determinant of tumor growth and metastasis. *Cancer Res* **76**, 5201–5208 (2016).

20. Godet, I. *et al.* Fate-mapping post-hypoxic tumor cells reveals a ROS-resistant phenotype that promotes metastasis. *Nat Commun* **10**, 4862 (2019).

21. Vaupel, P., Kallinowski, F. & Okunieff, P. Blood flow, oxygen and nutrient supply, and metabolic microenvironment of human tumors: a review. *Cancer Res* **49**, 6449–65 (1989).

22. Gatenby, R. A. & Gillies, R. J. A microenvironmental model of carcinogenesis. *Nat Rev Cancer* **8**, 56–61 (2008).

23. Lyssiotis, C. A. & Kimmelman, A. C. Metabolic Interactions in the Tumor Microenvironment. *Trends Cell Biol* **27**, 863–875 (2017).

24. Hobson-Gutierrez, S. A. & Carmona-Fontaine, C. The metabolic axis of macrophage and immune cell polarization. *Dis Model Mech* **11**, dmm034462 (2018).

25. Bader, J. E., Voss, K. & Rathmell, J. C. Targeting Metabolism to Improve the Tumor Microenvironment for Cancer Immunotherapy. *Mol Cell* **78**, 1019–1033 (2020).

26. Condeelis, J. & Pollard, J. W. Macrophages: Obligate Partners for Tumor Cell Migration, Invasion, and Metastasis. *Cell* **124**, 263–266 (2006).

27. Noy, R. & Pollard, J. W. Tumor-Associated Macrophages: From Mechanisms to Therapy. *Immunity* **41**, 49–61 (2014).

28. Linde, N. *et al.* Macrophages orchestrate breast cancer early dissemination and metastasis. *Nat Commun* **9**, 21 (2018).

29. Wenes, M. *et al.* Macrophage Metabolism Controls Tumor Blood Vessel Morphogenesis and Metastasis. *Cell Metab* **24**, 701–715 (2016).

30. Gould, S. E., Junttila, M. R. & de Sauvage, F. J. Translational value of mouse models in oncology drug development. *Nature Medicine 2015 21:5* **21**, 431–439 (2015).

31. Day, C. P., Merlino, G. & van Dyke, T. Preclinical Mouse Cancer Models: A Maze of Opportunities and Challenges. *Cell* **163**, 39–53 (2015).

32. Janská, L. *et al.* The MEMIC is an ex vivo system to model the complexity of the tumor microenvironment. *DMM Disease Models and Mechanisms* **14**, (2021).

33. Carmona-Fontaine, C. *et al.* Metabolic origins of spatial organization in the tumor microenvironment. *Proceedings of the National Academy of Sciences* **114**, 2934–2939 (2017).

34. Carmona-Fontaine, C. *et al.* Emergence of spatial structure in the tumor microenvironment due to the Warburg effect. *Proceedings of the National Academy of Sciences* **110**, 19402–19407 (2013).

35. Sánchez-Rivera, F. J. *et al.* Rapid modelling of cooperating genetic events in cancer through somatic genome editing. *Nature* **516**, 428–431 (2014).

36. Wang, R. *et al.* Hypoxia-inducible factor-dependent ADAM12 expression mediates breast cancer invasion and metastasis. *Proc Natl Acad Sci U S A* **118**, e2020490118 (2021).

37. Lehmann, S. *et al.* Hypoxia Induces a HIF-1-Dependent Transition from Collective-to-Amoeboid Dissemination in Epithelial Cancer Cells. *Current Biology* **27**, 392–400 (2017).

38. Pennacchietti, S. *et al.* Hypoxia promotes invasive growth by transcriptional activation of the met protooncogene. *Cancer Cell* **3**, 347–361 (2003).

39. Chen, J., Imanaka, N., Chen, J. & Griffin, J. D. Hypoxia potentiates Notch signaling in breast cancer leading to decreased E-cadherin expression and increased cell migration and invasion. *British Journal of Cancer 2010 102:2* **102**, 351–360 (2009).

40. Mardia, K. v. & Jupp, P. E. *Directional statistics*. (J. Wiley, 2000).

41. Collins, T. A., Yeoman, B. M. & Katira, P. To lead or to herd: optimal strategies for 3D collective migration of cell clusters. *Biomech Model Mechanobiol* **19**, 1551–1564 (2020).

42. Fraley, S. I. *et al.* Three-dimensional matrix fiber alignment modulates cell migration and MT1-MMP utility by spatially and temporally directing protrusions OPEN. *Scientific RepoRts |* **5**, 14580 (2015).

43. Ros, M. *et al.* ER-resident oxidoreductases are glycosylated and trafficked to the cell surface to promote matrix degradation by tumour cells. *Nature Cell Biology 2020 22:11* **22**, 1371–1381 (2020).

44. Sloane, B. F., Sameni, M., Podgorski, I., Cavallo-Medved, D. & Moin, K. Functional Imaging of Tumor Proteolysis. *Annu Rev Pharmacol Toxicol* **46**, 301–315 (2006).

45. Guillot, C. & Lecuit, T. Mechanics of epithelial tissue homeostasis and morphogenesis. *Science (1979)* **340**, 1185–1189 (2013).

46. Niessen, C. M., Leckband, D. & Yap, A. S. Tissue organization by cadherin adhesion molecules: Dynamic Molecular and Cellular Mechanisms of Morphogenetic Regulation. *Physiol Rev* **91**, 691–731 (2011).

47. Polyak, K. & Weinberg, R. A. Transitions between epithelial and mesenchymal states: acquisition of malignant and stem cell traits. *Nature Reviews Cancer 2009 9:4* **9**, 265–273 (2009).

48. Scheel, C., Onder, T., Karnoub, A., Weinberg, R. A. & Talmadge, J. E. Adaptation versus Selection: The Origins of Metastatic Behavior. *Cancer Res* **67**, 11476–11480 (2007).

49. Padmanaban, V. *et al.* E-cadherin is required for metastasis in multiple models of breast cancer. *Nature* **573**, 439–444 (2019).

50. Dongre, A. & Weinberg, R. A. New insights into the mechanisms of epithelial–mesenchymal transition and implications for cancer. *Nat Rev Mol Cell Biol* **20**, 69–84 (2018).

51. Jiang, L. *et al.* Metabolic reprogramming during TGFβ1-induced epithelial-to-mesenchymal transition. *Oncogene 2015 34:30* **34**, 3908–3916 (2014).

52. Glazier, J. A. & Graner, F. Simulation of the differential adhesion driven rearrangement of biological cells. *Phys Rev E* **47**, 2128 (1993).

53. Graner, F. & Glazier, J. A. Simulation of biological cell sorting using a two-dimensional extended Potts model. *Phys Rev Lett* **69**, 2013 (1992).

54. Szabó, A. & Merks, R. M. H. Cellular Potts modeling of tumor growth, tumor invasion, and tumor evolution. *Front Oncol* **3 APR**, 87 (2013).

55. Gordan, J. D. & Simon, M. C. Hypoxia-inducible factors: central regulators of the tumor phenotype. *Curr Opin Genet Dev* **17**, 71–77 (2007).

56. Wong, C. C.-L. *et al.* Hypoxia-inducible factor 1 is a master regulator of breast cancer metastatic niche formation. *Proc Natl Acad Sci U S A* **108**, 16369–74 (2011).

57. Gocheva, V. *et al.* IL-4 induces cathepsin protease activity in tumor-associated macrophages to promote cancer growth and invasion. *Genes Dev* **24**, 241–255 (2010).

58. Colegio, O. R. *et al.* Functional polarization of tumour-associated macrophages by tumour-derived lactic acid. *Nature* **513**, 559–563 (2014).

59. Bronte, V. & Murray, P. J. Understanding local macrophage phenotypes in disease: modulating macrophage function to treat cancer. *Nat Med* **21**, 117–119 (2015).

60. Weaver, B. A. How Taxol/paclitaxel kills cancer cells. *Mol Biol Cell* **25**, 2677–2681 (2014).

61. Belotti, D. *et al.* Paclitaxel (Taxol#{174}) Inhibits Motility of Paclitaxel-resistant Human Ovarian Carcinoma Cells'. **2**, 1725–1730 (1996).

62. Wang, X., Decker, C. C., Zechner, L., Krstin, S. & Wink, M. In vitro wound healing of tumor cells: Inhibition of cell migration by selected cytotoxic alkaloids. *BMC Pharmacol Toxicol* **20**, 1–12 (2019).

63. Gould, S. E., Junttila, M. R. & Sauvage, F. J. de. Translational value of mouse models in oncology drug development. *Nat Med* **21**, 431–9 (2015).

64. Bert, B. *et al.* Rethinking 3R strategies: Digging deeper into AnimalTestInfo promotes transparency in in vivo biomedical research. *PLoS Biol* **15**, e2003217 (2017).

65. Bressers, S. *et al.* Policy driven changes in animal research practices: mapping researchers' attitudes towards animal-free innovations using the Netherlands as an example. *Res Integr Peer Rev* **4**, 8 (2019).

66. Püschel, F. *et al.* Starvation and antimetabolic therapy promote cytokine release and recruitment of immune cells. *Proc Natl Acad Sci U S A* **117**, 9932–9941 (2020).

67. Nieto, M. A. 50+ shades of EMT in 20 years of embryo–cancer bonding. *Nature Reviews Molecular Cell Biology 2020 21:10* **21**, 563–563 (2020).

68. Dongre, A. & Weinberg, R. A. New insights into the mechanisms of epithelial–mesenchymal transition and implications for cancer. *Nature Reviews Molecular Cell Biology 2018 20:2* **20**, 69–84 (2018).

69. Chen, J., Imanaka, N., Chen, J. & Griffin, J. D. Hypoxia potentiates Notch signaling in breast cancer leading to decreased E-cadherin expression and increased cell migration and invasion. *Br J Cancer* **102**, 351–60 (2009).

70. Wadhams, G. H. & Armitage, J. P. Making sense of it all: bacterial chemotaxis. *Nature Reviews Molecular Cell Biology 2004 5:12* **5**, 1024–1037 (2004).

71. Gerisch, G. Chemotaxis in Dictyostelium. *https://doi.org/10.1146/annurev.ph.44.030182.002535* **Vol. 44**, 535–552 (2003).

72. Labuschagne, C. F., Cheung, E. C., Blagih, J., Domart, M.-C. & Vousden, K. H. Cell Clustering Promotes a Metabolic Switch that Supports Metastatic Colonization. *Cell Metab* **30**, 720-734.e5 (2019).

73. Dewhirst, M. W. & Secomb, T. W. Transport of drugs from blood vessels to tumour tissue. *Nature Reviews Cancer 2017 17:12* **17**, 738–750 (2017).

74. Jeong, J. Y. *et al.* One-step sequence-and ligation-independent cloning as a rapid and versatile cloning method for functional genomics Studies. *Appl Environ Microbiol* **78**, 5440–5443 (2012).

75. Vinci, M., Box, C., Zimmermann, M. & Eccles, S. A. Tumor spheroid-based migration assays for evaluation of therapeutic agents. *Methods in Molecular Biology* **986**, 253–266 (2013).

76. Tsuyoshi Hirashima. Primer for cellular Potts model. *https://www.mathworks.com/matlabcentral/fileexchange/64207-primer-for-cellular-potts-model*.

FIGURE LEGENDS

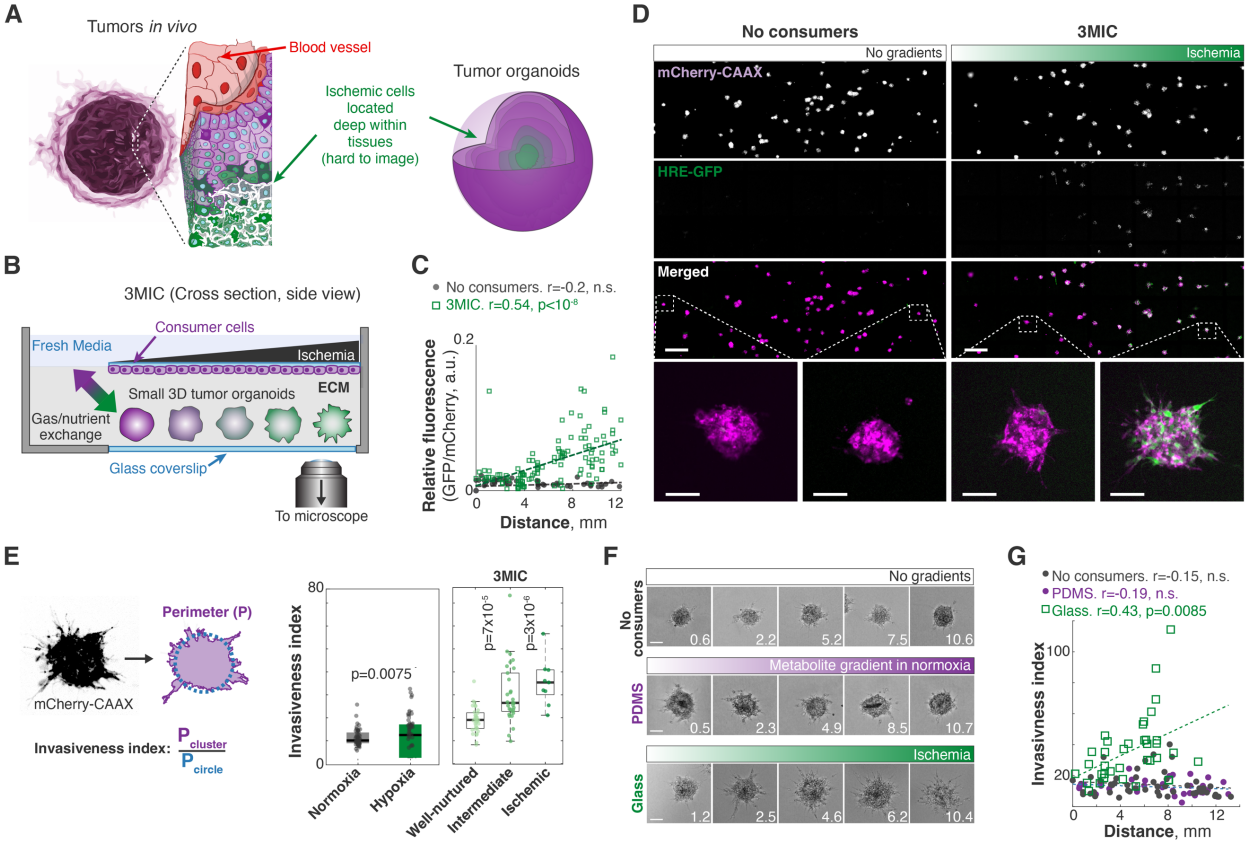

Figure 1: Design and implementation of a metabolic microenvironment chamber for 3D cultures.
A. Schematic showing that in solid tumor and conventional tumor organoids. Metastases often emerge from ischemic regions that are hard to access and image in these systems.
B. Schematic cross-section of the 3MIC. In this system, a monolayer of "consumer" cells grows on the top coverslip. Tumor spheroids grow underneath these cells embedded in ECM and are enclosed in a small space connected only one side through (left) to a large reservoir of fresh media.
C. *Per* spheroid GFP levels of HRE-GFP lung KP cells cultured in the 3MIC. GFP levels are a proxy for hypoxia and are. Normalized to constitutive mCherry-CAAX signal. Dashed line: linear fit.
D. Whole-3MIC images showing GFP and mCherry fluorescence in tumor spheroids cultured alone (left column) or in the presence of consumer cells (right column). Bottom panels highlight representative tumor spheroids. Bars: 1000μm, 100μm for insets.
E. We defined invasiveness index, as the perimeter of tumor spheroid over the perimeter of a circle with the same area. Using this index, we quantified the invasiveness of lung KP cluster under different environments. Well-nurtured, intermediate, and ischemic condition correspond to different regions of the 3MIC. Data points: per spheroid invasiveness.
F. Representative images of individual Lung KP spheroids grown Lung KP spheroids for 24h in the absence of consumer cells (top), or in consumer cells in PDMS- or glass-based 3MICs (center and bottom). Numbers in lower right corner denote the distance to the opening in mm. Bars:100μm
G. Quantification of experiment shown in (**F**). Data points: invasiveness index of individual spheroids. Dash lines: linear fit.

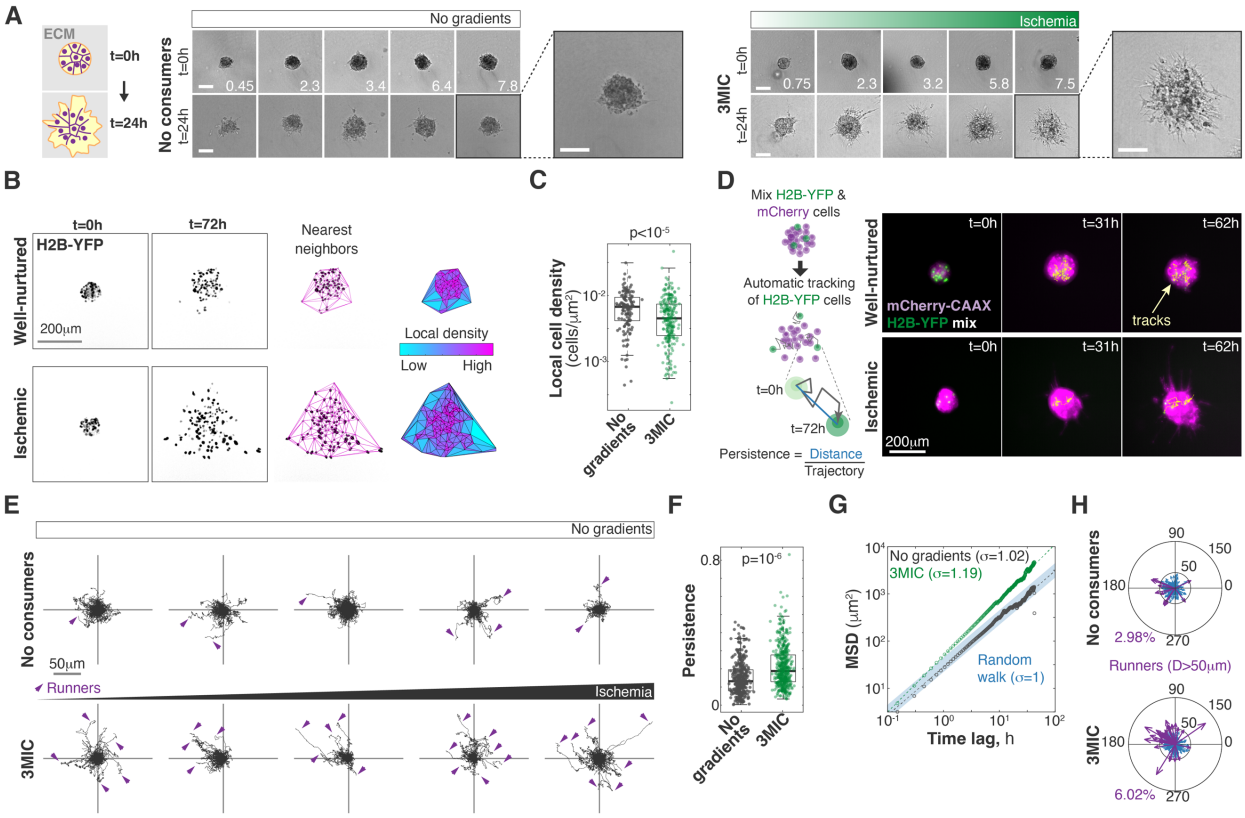

Figure 2: Ischemic cells in the 3MIC migrate more.

A. Left: Schematic showing the experimental design. Center: Lung KP spheroids imaged after 0h (top) and 24h (bottom) of growth in different regions of the 3MIC but without consumer cells. These clusters grew uniformly and retained smooth round shapes. Right: Same data but for spheroids grown in the presence of consumer cells. Ischemic spheroids grew larger and more protrusive. Numbers in lower right corner denote the distance to the opening in mm. Bars: 100μm.

B. Image-based method to estimate local cell density. We first located individual cells expressing a fluorescent nuclear marker (H2B-YFP). Then we triangulated closest neighbors and estimated areas between these neighbors. Cell density is the inverse of the area.

C. Cells in ischemic spheroids disperse more with a larger decrease in local cell density.

D. Schematic depicting the experimental setup for chimeric spheroids formed by cells expressing different fluorophores. We then tracked individual cells and calculated their speed, direction, and persistence (final distance/trajectory). Representative images show randomly selected cell tracks.

E. Tracks of individual cells centered at their respective origins. Tracks in top 5 plots came from 5 different tumor spheroids located at various distances along the 3MIC but in the absence of consumer cells. Lower 5 plots show tracks of 5 clusters at similar distances as the plots above but in the presence of consumer cells. Arrowheads show tracks of runner (defined as having a net displacement of 50μm or more).

F. Persistence of individual cells. Cells in ischemic spheroids are significantly more persistent than cells in well-nurtured spheroids.

G. Mean-squared displacement (MSD) analysis of all tracked cells. Ischemic cells show superdiffusivity (α>1), *i.e.* they disperse more than the random expectation. This is consistent with their higher persistence.

H. Compass plots showing the direction and magnitude of final displacement. Runner cells highlighted in purple. Ischemic cells show a small bias towards high nutrients levels (left).

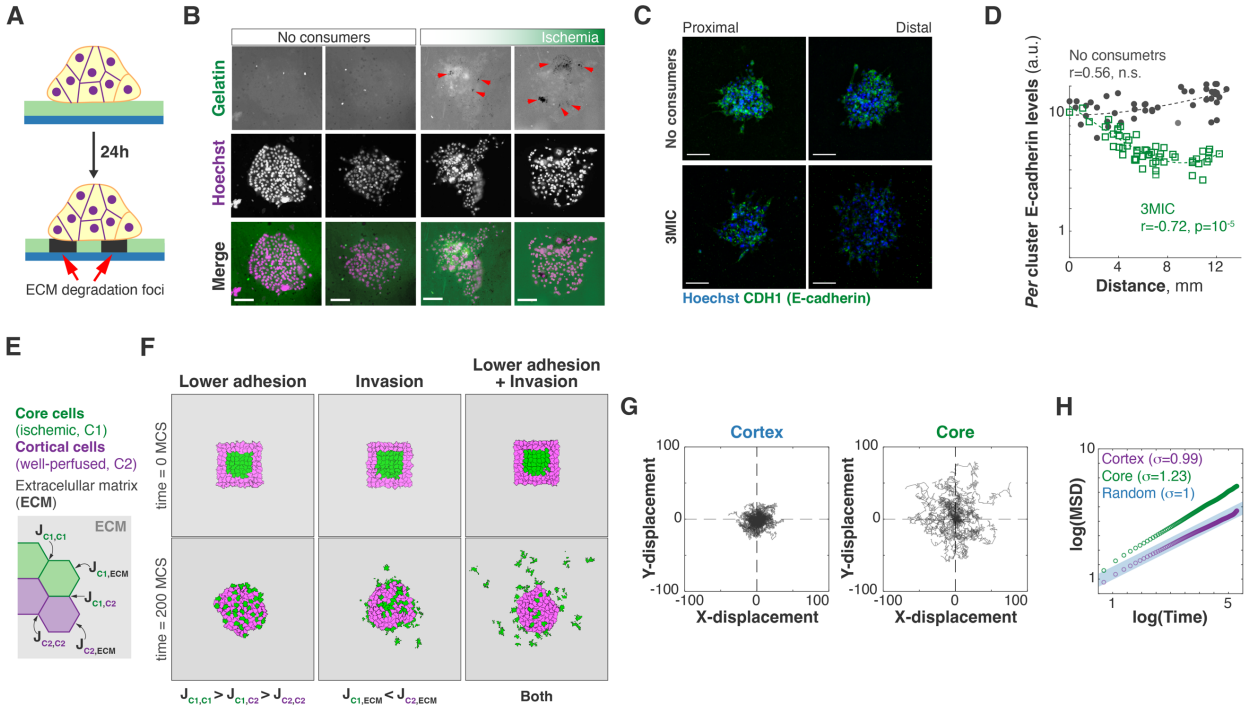

Figure 3: Computer simulations suggest that a decrease in epithelial adhesion and increased invasion synergize to disperse tumor cells.

A. Schematic depicting gelatin degradation assay.

B. Representative images of spheroids grown on gelatin coated surface under no gradient and 3MIC conditions. Ischemic spheroids show much higher gelatin degradation (dark regions, red arrowheads). Bars: 100μm.

C. Representative images of lung KP spheroids grown in the 3MIC and immunostained for E-cadherin (green). Nuclei stained with Hoechst (blue). Bars: 100μm.

D. E-cadherin levels decrease with ischemia gradient. Data points: per spheroid E-Cad levels. Dashed line: linear fit. Bars: 100 μm.

E. We simulated the behaviors of ischemic (core, green) cells and well-nurtured (cortical, magenta) cells using a Cellular Potts Model. See more details in main text and supplementary information.

F. Initial and final conditions of simulated tumor populations simulations under different rules. We found that the combination of lower epithelial adhesion and invasion, but not each process alone, capture the main features of our experimental data.

G. Tracks of simulated ischemic (core) and well-nurtured (cortical) cells. In the lower epithelial adhesion and invasion show a remarkably similar pattern to tracks obtained from microscopy time-lapse tracking of individual cell movement.

H. MSD of simulated well-nurtured and ischemic cells with lower epithelial adhesion and invasion. MSD data is in the same order of magnitude as experimental data (Fig. 2G).

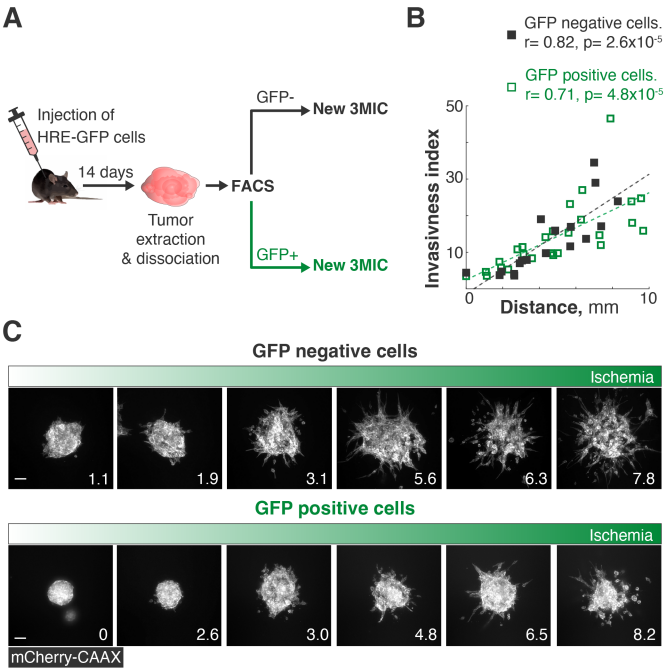

Figure 4: Ischemia induced invasiveness is a phenotypic change.
A. Lung KP cells expressing HRE-GFP and mCherry-CAAX were injected subcutaneously in C57BL/6 mice and allowed to grow for 14 days. These syngeneic tumors were extracted and FACS-sorted into GFP positive (hypoxic/ischemic) and GFP negative (normoxic/well-nurtured) populations. These different sub-populations were then grown as tumor spheroids in 3MICs in the absence or presence of consumer cells.
B. Quantification of invasiveness of experimental setup shown in (**A**). Squares show the invasiveness indexes of individual spheroids. Dashed lines: linear fit. We observed that ischemia in the 3MIC increased invasion in spheroids derived from both, well-nurtured and ischemic tumor regions.
C. Representative images of tumor spheroids growing at different locations of 3MICs. Numbers in lower right corner denote the distance to the opening in mm. Bars: 100μm.

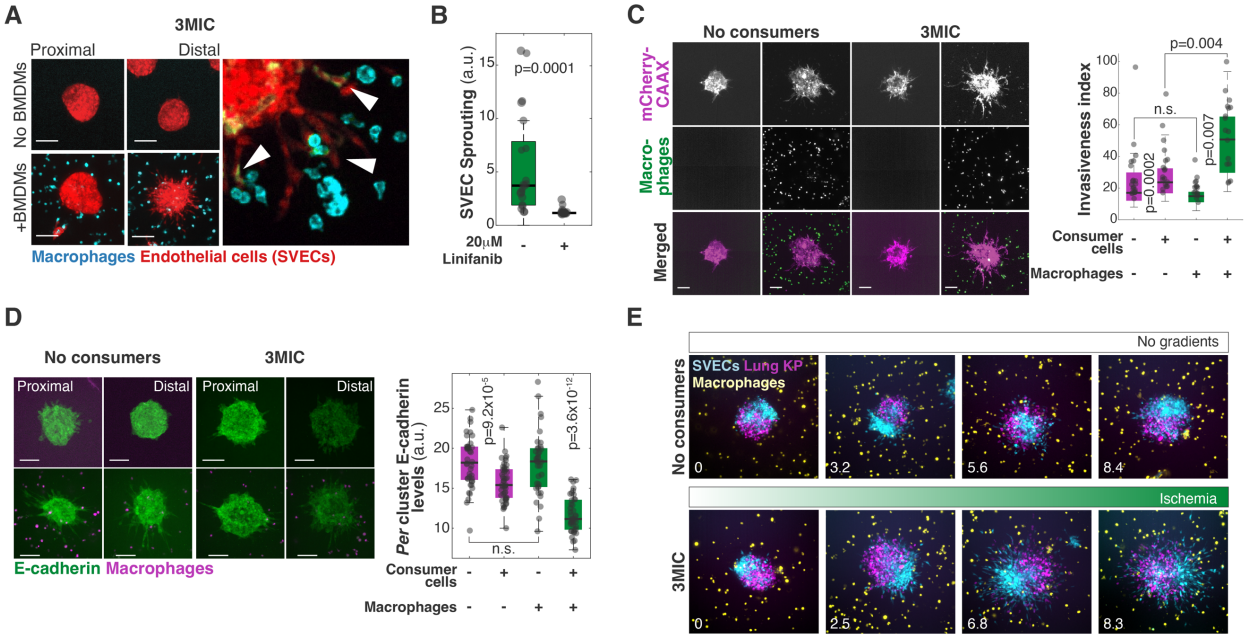

Figure 5: Coculture of different cells in 3MIC.

A. Clusters of endothelial cells (SVECs, red) grown in 3MICs in the presence or absence of BMDMs (cyan). Ischemic macrophages induced sprouting in SVEC clusters suggesting induction of angiogenesis. Bars: 100 μm.

B. Quantification of induction of SVEC sprouting by BMDMs with or without VEGFA inhibition (Linifanib).

C. Representative images and quantification of invasiveness of Lung KP spheroids co-cultured with BMDMs in the 3MIC. Ischemic macrophages significantly enhance tumor invasiveness. Data points: *Per* spheroid invasiveness. Bars: 100μm.

D. Representative images of lung KP spheroids grown in the 3MIC and immunostained for E-cadherin (green) and in the presence or absence of macrophages (magenta). Note that ischemia and macrophages synergize in their reduction of E-Cad levels. Bars: 100 μm.

E. Representative images of triple co-cultures: Chimeric Lung KP cells and SVEC spheroids, were grown in the presence of BMDMs under no gradient conditions and 3MIC. Numbers in lower right corner denote the distance to the opening in mm. Bars: 100μm.

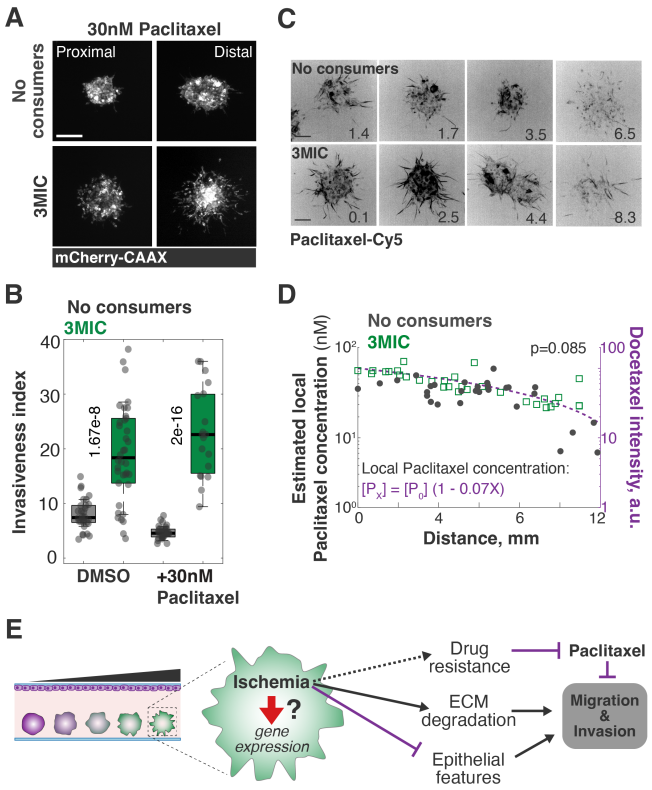

Figure 6: Ischemia induces chemoresistance in ischemic spheroids.
A. Representative images of Lung KP spheroids grown in the presence and absence of 30nM Paclitaxel, showing ischemic spheroids retained migratory capacity. Bars: 100μm.
B. Quantification of (**A**). Points: invasiveness of individual clusters.
C. Representative images of Lung KP clusters grown in the 3MIC in the presence or absence of gradients and treated with a fluorescent paclitaxel analog (Docetaxel-Cy5). We used levels of this dye to estimate local levels of the drug in the 3MIC. Numbers in lower right corner denote the distance to the opening in mm. Bars: 100μm.
D. Estimated levels of paclitaxel in the presence or absence of consumer cells. While diffusion did play a role in decreasing drug levels in both conditions, consumer cells did not. Thus, differential response to paclitaxel cannot be due to lower drug availability but triggered by some ischemia-related process.
E. Summary: ischemia enhanced ECM degradation increasing tumor invasion. This environment also leads to paclitaxel resistance.